

# Experimental study of thiophene and ferrocene in synthesis of single-walled carbon nanotubes in rich premixed hydrogen/air flames

Cen Zhang<sup>a,e,\*</sup>, Bo Tian<sup>a,d,\*\*</sup>, Cheng Tung Chong<sup>b</sup>, Boning Ding<sup>c</sup>, Luming Fan<sup>a</sup>, Xin Chang<sup>a</sup>, Simone Hochgreb<sup>a</sup>

<sup>a</sup>*Department of Engineering, University of Cambridge, Cambridge CB2 1PZ, United Kingdom*

<sup>b</sup>*China-UK Low Carbon College, Shanghai Jiao Tong University, No. 3 Yinlian Rd, Pudong New District, Shanghai 201306, China*

<sup>c</sup>*Department of Materials Science and Metallurgy, University of Cambridge, 27 Charles Babbage Road, Cambridge CB3 0FS, United Kingdom*

<sup>d</sup>*College of Engineering and Technology, University of Derby, Markeaton Street, Derby DE22 3AW, United Kingdom*

<sup>e</sup>*CNOOC Energy Economics Institute, Dongcheng District, Beijing 100013, China*

---

## Abstract

The effects of varying concentrations of ferrocene and thiophene on the synthesis of carbon nanotubes (CNT) in a floating catalyst, flame-based reaction system were investigated. Pre-vapourised ethanol was used as CNT feedstock, and a surrounding premixed H<sub>2</sub>/air flames was used as the heat source. Samples of the synthesised material were collected and analysed using Raman spectroscopy, scanning electron microscopy, and transmission electron microscopy to determine the properties of the collected CNT samples. Sulphur to iron mass ratios were varied from 0 up to 10.1, by changing the relative amounts of thiophene and ferrocene. The latter was found to

---

\*Corresponding author.

\*\*Corresponding author.

*Email addresses:* cz299@cantab.ac.uk (Cen Zhang), bt312@cam.ac.uk (Bo Tian)

have only a marginal effect on the improvement in the yield of CNTs, but led to enhanced yield of iron oxide nanoparticles. In comparison, the addition of sulphur exhibited an increase in the synthesis of CNTs as compared to iron oxide nanoparticles, including their number density and length. An optimum window of mass ratios  $m_{S/Fe}$  at 0.1–2 was identified. A numerical model for the diffusion of species is coupled with an equilibrium chemical model for the resulting species to understand the mechanism of the synthesis process, showing the range of elemental proportion conditions and residence times favourable to high yield of CNTs.

*Keywords:*

Flame synthesis, Carbon nanotubes, Premixed flame

---

## 1. Introduction

Carbon nanotubes (CNTs) are one-dimensional nanomaterials known to possess superior physical properties, including high mechanical strength and flexibility [1], superb electrical [2] and thermal conductivity [3], thermochemical stability and compatibility with processing in solution. The excellent properties have attracted much scrutiny for a broad range of potential applications. CNTs, often used as additives to improve the performance of base materials, have been applied to a wide range of devices such as mechanically and electrically enhanced polymer composites [4–7], electrodes [8], multifunctional coatings [9] and ultra-thin films [10]. The growing demand in the fields of electronics and semiconductors, energy, battery and capacitors, advanced materials are expected to fuel the growth of the CNT market. In view of the growing demand, significant efforts are needed to achieve production

of low-cost CNT with high crystallinity to further enable its application in various technological sectors [11].

Despite the popularity of using chemical vapour deposition (CVD) for CNT production [12–14], flame-assisted methods have gained increasing attention as an alternative technique for CNT synthesis that can significantly increase the rate of production in the form of continuous rather than batch methods [15]. Flame synthesis is a continuous-flow, scalable method with potential for high throughput and lower production cost as compared to other known synthesis methods such as CVD [1], laser ablation [16] and arc discharge [17]. There has been a long history of carbon material production using flames, and the mass production of many commercial products, including carbon black, fumed silica and titanium dioxide pigment, have already been realised by flame methods [18]. Trace amounts of CNTs were first reported by Howard *et al.* while using premixed hydrocarbon/oxygen flames [19]. Thereafter, various flame configurations have been developed for producing CNTs, which can be categorised into two classes based on the type of flames in use, namely diffusion flames [20–22], and premixed flames [23–27].

Regardless of geometrical configuration, a stable and constant heat supply must be ensured. Carbon sources in appropriate amounts must be carefully selected, and catalysts, typically metal or metal-containing compounds (*e.g.* iron [27, 28] and nickel [29, 30]), and/or sulphur-containing compounds (*e.g.* thiophene), also play critical roles in the process for a successful synthesis. Many researchers have investigated the role of metal catalysts, and it is widely-accepted that the metal nanoparticles whose surfaces are activated or deliquescent at high temperatures provide sites for the inception and growth

of CNTs. The effect of varying concentrations of metal catalysts in CNT synthesis has been reported both in CVD and flame synthesis processes. Li *et al.* investigated the effects of ferrocene and thiophene on CNT synthesis in a floating catalyst CVD system using ethanol as carbon sources [13, 31] in an electrically heated furnace with hydrogen as the bath gas. They identified an optimum range of ferrocene concentrations as 0.2–2.5 wt.% within which the process seemed insensitive to the variation of ferrocene. Nonetheless, the process showed a marked sensitivity to thiophene concentrations. The optimum concentration of thiophene was found to be around 0.5 wt.%, at which aerogels of highly crystalline single-walled carbon nanotubes (SWCNTs) could be produced, with a product purity greater than 96 wt.% were attained. Chaisitsak *et.al* [32] systematically studied the influence of the ratio of ferrocene to ethanol on the CNT synthesis a similar furnace system to be in the range of 0.1-3.0 wt.%. Although CNTs were observed throughout the whole range, the optimum condition was identified as 1.0-1.5 wt.% where highly crystalline SWCNTs with fewer amorphous impurities were obtained. They concluded that the ratio of ferrocene to ethanol predominantly affects the formation of impurities and the crystallinity of CNTs.

Experimental studies have revealed that the yield of CNTs can be significantly enhanced by adding sulphur into CNT production process in floating catalyst furnaces [13, 33–37]. In the 1990s, Tibbetts *et al.* [38] discovered that sulphur promotes the formation of carbon filaments due to the ability of liquefying the catalytically active iron particles. Moreover, they noticed that higher sulphur concentration decreases the filaments' quality in terms of length and straightness. This was attributed to the elevated melting point of

the particles beyond the eutectic, thus impeding filament growth. However, a further investigation by the same author [39] contradicted the previous claim and reported that an enhanced yield of CNT fibres was observed experimentally at temperatures up to 1208 °C, beyond the Fe-C eutectic temperature (1153 °C [40]). They concluded that sulphur promotes the dissolution of carbon into catalyst nanoparticles [39]. Motta *et al.* extended the study of sulphur in CNT synthesis and confirmed sulphur's role of promoting lengthening and entanglement of CNTs [40, 41]. Furthermore, their experiments revealed that in the absence of sulphur, most iron catalyst particles formed at high temperatures were encapsulated by layered carbon, which appeared to deactivate the catalyst particles [40]. They pointed out that sulphur has two distinct roles: one is to enhance CNT growth by surface diffusion, while the other is to promote the assembly of carbon atoms onto CNT edges [40]. More recently, Yuan *et al.* [42] reported sulphur-induced chirality changes while studying the role sulphur in an ethanol CVD process. Although minor addition of sulphur-containing compounds (0.0001 wt.% carbon disulfide or 0.001 wt.% thiophene in ethanol) only helped improve the CNT yield, chiral selectivity became manifest as the concentration of the sulphur-containing compounds further increased, in particular when thiophene reached 0.1 wt.% [42]. The possible cause was claimed to be the selective blocking of active sites on the metal catalyst particles.

The role of sulphur in CNT production has rarely been investigated in flame synthesis, although a couple of studies related to the role of sulphur in flame synthesis have been attempted. Vander Wal *et al.* tested the effect of sulphur in a "pyrolysis flame", in which where a steel tube placed was 1 cm

above a flat flame McKenna burner fueled by a fuel-rich air/C<sub>2</sub>H<sub>2</sub> [29]. Their results showed that neither the yield nor the morphology of the CNT products was improved by the addition of 0.8 vol.% thiophene in the reactant gases. A more recent study by Okada *et al.* [43] fed sulphur vapour with ferrocene with a sulphur/ferrocene mass ratio of 20 into a premixed Bunsen flame of diluted C<sub>2</sub>H<sub>4</sub>/O<sub>2</sub>/Ar ( $\phi = 1.05$ ) to produce CNTs. Although high purity (carbon of 90 wt.%), single-walled CNTs of an average diameter of 0.96 nm were reported, no discussion of the role of sulphur was mentioned. As to the effect of sulphur, the following questions arise: does adding sulphur (thiophene) into a combustion system for CNT production have the same effectiveness as that in a CVD reactor? And what might be the differences between these two processes regarding the addition of ferrocene and thiophene?

In the present study, we explore the growth potential of CNTs using thiophene and ferrocene as the source of catalysts. A pilot ethanol jet serves as carbon source, and a carbon-free hydrogen-rich flame provides the heat for the reaction as a co-flow surrounding the reactant mixture of ethanol, thiophene and ferrocene. The effect of sulphur as a precursor for CNT growth is investigated, and the morphology of the CNT material produced is examined. The potential of the flame synthesis method for high quality CNT production and throughput is discussed.

## 2. Experimental

The schematic of the experimental setup is illustrated in Fig. 1. Details of the system can be found in a previous paper [44], while we here briefly describe the arrangements. The system consists of a premixed flat flame

burner with a sintered copper ring (50 mm O.D., 10 mm I.D.) for stabilising H<sub>2</sub>/air flames. An alumina tube (10 mm O.D, 6 mm I.D.) was installed at the centre for CNT reactant injection. The outlet of the central tube was placed 5 mm above the burner plate to avoid burnout of reactant. A clear fused quartz tube (75 mm O.D., 70 mm I.D.) surrounded the burner plate enclosing the reacting environment. All gas flows were regulated by mass flow controllers (Alicat Scientific, MC-500SCCM-D for Argon, MC-10SLPM-D for H<sub>2</sub> and CH<sub>4</sub>, MC-20SLPM-D for air), and the injection of liquid reactants for the synthesis was controlled by a syringe pump (World Precision Instruments). The reactants, consisting of varying proportions of ethanol (the carbon source), ferrocene and thiophene, were fed into a fabricated shear-based atomiser. The atomised droplets were carried by a stream of argon into a temperature-controlled heated pipeline (maintained at 100 °C) for the subsequent synthesis.

~~Operating conditions for the operating H<sub>2</sub>/air were constrained to rich premixed regions of  $\phi$ , from 1.05–1.2 to maximize reaction and minimize oxidation.~~<sup>R2</sup> Our previous study [44] demonstrated that a slightly hydrogen-rich environment is favourable for CNT production, as little oxygen is left in the pyrolysis zone, which helps to avoid rapid oxidation of the catalyst Fe nanoparticles. Moreover, an slight excess of hydrogen can significantly suppress the formation of soot nanoparticles and hence enhance the yield of CNTs. On the other hand, excessive hydrogen can have negative effects on CNT formation, as H radicals suppress the formation of SP<sup>2</sup> graphitic structure [45] by converting C into gas phase substances [46]. Thus, a optimum equivalence ratio window  $\phi$  of 1.05–1.2 of the surrounding flame identified in

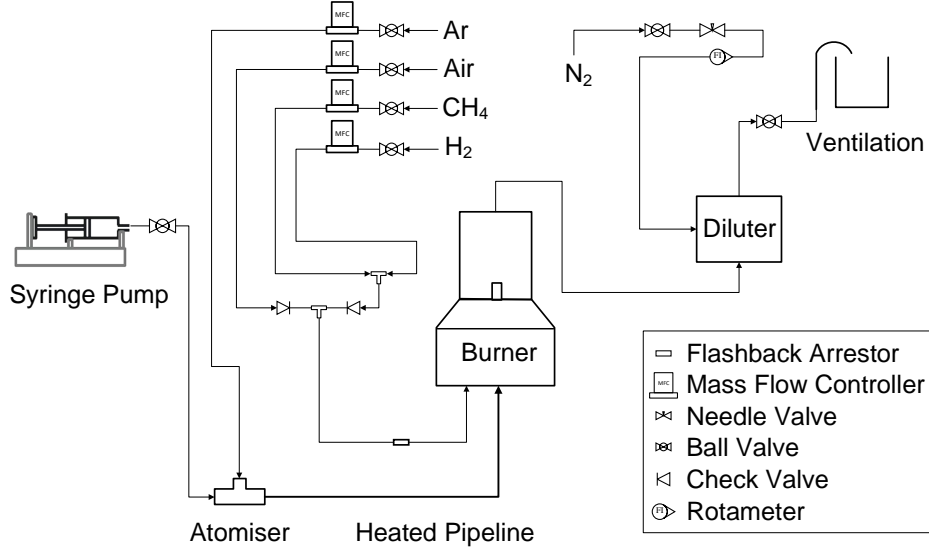


Figure 1: Schematic of the experimental setup.

our previous study [44] was selected.<sup>R2</sup> A trace amount of CH<sub>4</sub> (0.4 vol.% in mixtures) was intentionally doped into the H<sub>2</sub>/air mixtures to help visualise flame fronts as a safety precaution. The reactant injection rate and the argon flow rate were fixed at 0.5 mL/min~~ml/min~~<sup>R3</sup> and 0.1 slpm, respectively, ~~which was an optimal combination of parameters for CNT synthesis found in our previous study [44]<sup>R2</sup>~~. A stainless steel probe (6 mm O.D., 3 mm I.D.) positioned at a height above burner (HAB) of 230 mm was used for collecting the as-produced nanomaterials onto a PTFE membrane filter (SKC Ltd, pore size 0.45 μm ). Three individual Raman spectroscopy measurements (HORIBA XploRA PLUS) were carried out using a 532 nm laser on each sample at random locations, covering a region with a diameter of roughly 1.2 μm each. The obtained Raman spectra were then normalised against their

respective global peak value before an averaged Raman spectrum for each sample was produced. The samples were further examined by X-ray diffraction (Empyrean) using a Cu anode, scanning electron microscopy (Zeiss Leo Gemini 1530VP FEG-SEM) and transmission electron microscopy (FEI Tecnai Osiris FEGTEM).

We examined 11 different reactant mixtures containing various proportions of catalyst precursors in ethanol solvents at different  $\phi$  from 1.05–1.2 as shown in Table 1).

Table 1: Experimental conditions for the study of catalysts. The flame equivalence ratio  $\phi$  was varied from 1.05–1.2, and the injection rate of ethanol was kept at 0.5 mL/min ml/min<sup>R3</sup> while the argon gas flow rate was maintained at 0.1 slpm.

Table 2: Experimental conditions

No.	Thiophene (wt.%)	Ferrocene (wt.%)	$m_{S/Fe}$ (-)
1	0	0.1	0
2	0	0.3	0
3	0	0.5	0
4	0	1.0	0
5	0	2.0	0
6	0	3.0	0
7	0.1	1.0	0.1
8	1.5	2.3	0.8
9	1.6	1.0	2.0
10	2.0	0.5	5.1
11	2.0	0.25	10.1

### 3. Numerical analysis

A series of calculations were performed to gain insight into the CNT synthesis processes, including temperatures and species distributions within

the reactor, and to better understand the mechanisms of the CNT formation, including estimates of the temperature and composition of the mixture in the product gases of the surrounding flame, via a 2-D axisymmetric model of the process of diffusion of products and reactants across the central layer.

### 3.1. 1-D reactor model

The flame temperature of the 1-D burner stabilised H<sub>2</sub>/air flame was estimated using the chemical kinetics GRI-Mech 3.0 [47] assisted by the open-source software, Cantera [48]. This software has a variety of tools for investigating processes involving chemical kinetics, thermodynamics, and transport. The flame temperature was calculated based on a constant burner temperature and at atmospheric pressure at an equivalence ratio equal to 1.05 as we did in our previous study [44].<sup>R2</sup> More details of the solution method can be found in Ref.[48, 49].

### 3.2. 2-D diffusion model

A 2-D model was developed which simulates the post-flame mixing between the centrally injected reactants (ethanol and argon), and the surrounding hot products (water and nitrogen) from the premixed hydrogen flame. The model is based on a co-flow diffusion flame model [50, 51], here applied for similar conditions. The gases are assumed to be ideal, and have the same transport properties. The model assumes identical diffusivity for all species and heat and ignore the energy equation for ethanol pyrolysis, so that the conservation equations for the reactant ethanol could be written as:

$$\rho u_z \frac{\partial Y_e}{\partial z} + \rho u_r \frac{1}{r} \frac{\partial}{\partial r} (r Y_e) = \frac{1}{r} \frac{\partial}{\partial r} \left( r \rho D_f \frac{\partial Y_e}{\partial r} \right) \quad (1)$$

where  $r$  is the radius from the centre;  $D_f$  is the diffusivity of the mixture.  $Y_e$  is the mass fraction of ethanol. The variables  $u_r$  and  $u_z$  are radial and axial gas velocity respectively. The the initial temperature of feedstock,  $T_{e,0}$ , is set to the measured value of 100 °C, and the surrounding hot gases,  $T_{i,0}$ , is set to 1471 °C. ~~from the 1-D Cantera flame model.~~<sup>R2</sup> The value of  $T_{i,0}$  is calculated based on a constant burner temperature of 25 °C and at atmospheric pressure as in our previous study [44]. Heat loss via conduction to surroundings was considered, but the radiation loss is not taken into account. <sup>R2</sup> A mixture fraction,  $\xi$ . is defined as the extent of mixing between the inner and outer streams:

$$\xi = \frac{Y_i - Y_{i,0}}{Y_{e,0} - Y_{i,0}} \quad (2)$$

where  $Y_i$  is the species mass fraction of species  $i$ ,  $Y_{e,0}$  and  $Y_{i,0}$  are the initial concentration of ethanol and species  $i$  respectively. By assuming uniform constant (with temperature) specific heats for the mixture assuming adiabatic mixing between the streams, we obtain an expression for the local temperature:

$$T = Y_e T_{e,0} + (1 - Y_e) T_{i,0} \quad (3)$$

The mass conservation equation in axisymmetric cylindrical coordinates is:

$$\frac{\partial}{\partial z} (\rho u_z) + \frac{1}{r} \frac{\partial}{\partial r} (r \rho u_r) = 0 \quad (4)$$

The momentum equations in both axial and radial directions are:

$$\rho u_z \frac{\partial u_z}{\partial z} + \rho u_r \frac{\partial u_z}{\partial r} = \frac{1}{r} \frac{\partial}{\partial r} \left( \mu r \frac{\partial u_z}{\partial r} \right) + \rho g \quad (5)$$

and

$$\rho u_r \frac{\partial u_r}{\partial r} + \rho u_z \frac{\partial u_r}{\partial z} = \mu \left[ \frac{1}{r} \frac{\partial}{\partial r} \left( r \frac{\partial u_r}{\partial r} \right) - \frac{u_r}{r^2} \right] \quad (6)$$

The density of the mixture at constant pressure conditions is:

$$\rho = \rho_{ref,0} \frac{T_0}{T} \frac{W}{W_{ref}} \quad (7)$$

where the subscript *ref* denotes a reference molecular weight. The molecular weight of the mixture is calculated based the flame products (25.7 wt.% H<sub>2</sub>O and 74.3 wt.% N<sub>2</sub>) emerging from the stabilised flame:

$$W = \left( \frac{0.743(1 - Y_e)}{W_{N_2}} + \frac{0.257(1 - Y_e)}{W_{H_2O}} + \frac{Y_e}{W_e} \right)^{-1} \quad (8)$$

The diffusivity of the mixture at 293 K is assumed to be equal to that of air, as in previous studies [52, 53].  $D_{ref} = 0.2 \times 10^{-4}$  m<sup>2</sup>/s [54], and the dependence on the temperature is [55]:

$$D_f = D_{ref} \left( \frac{T}{T_{ref}} \right)^{1.67} \quad (9)$$

The viscosity of the gaseous mixture is assumed to be that of the nitrogen at 300 K and 101 kPa:  $\mu_{v,ref} = 1.79 \times 10^{-5}$  Pa·s [56], and Sutherland's law [57] is used in the estimation of the dynamic viscosity of the mixture at different temperatures,

$$\mu_v = \mu_{v,ref} \frac{2.78T_{ref} + 8C_s}{2.78T + 8C_s} \left( \frac{T}{T_{ref}} \right)^{\frac{3}{2}} \quad (10)$$

where  $C_s$  is Sutherland's constant. The value of  $C_s = 120$  for standard air [58]. The numerical results are calculated for an outer flame equivalence

ratio of  $\phi = 1.05$ , where  $\text{H}_2$  and air are supplied at 7.0 slpm and 16.7 slpm, respectively, and results in a initial axial velocity of  $u_{i,0} = 0.6$  m/s and a temperature of 1471 °C. Ethanol vapour and argon are injected through the central tube at molar ratio of 38% and 62%, respectively. This yields an initial axial velocity for the central stream of  $u_{e,0} = 0.27$  m/s. Based on these initial assumptions, the 2-D model simulates the whole mixing process and uses the estimated flame temperatures as an input to model the spatial distribution of mixing temperatures and mixture fractions of the synthesis in an axisymmetrical domain and with boundary conditions as follows:

$$\begin{array}{llll}
 z = 0 & Y_e = 1 & u_z = u_{e,0} & u_r = 0 \text{ for } 0 \leq r \leq r_p \\
 & Y_e = 0 & u_z = u_{i,0} & u_r = 0 \text{ for } r > r_p \\
 z = \infty & Y_e = 0 & u_z = 0 & u_r = 0 \\
 r = 0 & \frac{\partial Y_e}{\partial r} = 0 & \frac{\partial u_z}{\partial r} = 0 & u_r = 0 \\
 r = \infty & Y_e = 0 & u_z = 0 & u_r = 0
 \end{array} \quad (11)$$

where  $r_p$  is the inner diameter of the inner port. Combining Eqs. (1) to (10) with the boundary conditions stated in Eq. (11) allows a solution for ethanol mass fraction  $Y_e$ , velocities  $u_z$  and  $u_r$ , and  $T$  to be obtained numerically.

### 3.3. Thermodynamic equilibrium calculations

The thermodynamic equilibrium of a mixture can be represented by a set of simultaneous non-linear equations connecting the thermodynamic properties of substances, subject to the laws of atomic conservation [59]. An equilibrium model was constructed containing H, C, O, S and Fe elements,

and 100 species in three phases (solid, liquid and gas).

Most of the species considered have well-established properties for condensed phase iron carbide,  $\text{Fe}_3\text{C}(\text{s})$  and  $\text{Fe}_3\text{C}(\text{l})$  were extracted from Burcat's thermodynamic database [60], as were the properties for gas phase thiophene,  $\text{C}_4\text{H}_4\text{S}(\text{g})$ , and ferrous sulphide,  $\text{FeS}(\text{g})$ . Cementite, or  $\text{Fe}_3\text{C}$ , is a metastable phase and it is very likely to decompose into Fe and graphite at higher temperatures beyond its melting point [61, 62]. Thermodynamic properties of ferrocene,  $\text{Fe}(\text{C}_5\text{H}_5)_2$ , were extracted from Fulem *et al.*'s theoretical estimations [63].<sup>R2</sup>

Thermodynamic data for CNTs in literature are rather scarce, and the governing factors that determine the thermodynamic properties of CNTs have yet to be systematically investigated. However, experimental studies on CNTs by Pradhan *et al.* [64] showed that the specific heat capacity of multi-walled CNTs (MWCNTs) and single-walled CNTs with different orientations were within 7% of those of graphite powder. Kabo *et al.* [65] used an adiabatic calorimeter to determine that the ratio of heat capacities of MWCNTs to graphite was 1.03 between 300 and 370 K, and predicted that the specific heat capacity of MWCNTs resembles that of graphite beyond 370 K. By referring the thermodynamic properties of CNTs measured by Kabo *et al.* [65], we found the Gibbs free energy of CNTs resemble closely to that of graphite between 300 and 2200 K. Based on these findings, we selected graphite as a reasonable representation of all solid carbon products in the simulations, under the symbol of  $\text{C}(\text{s})$  [65, 66].<sup>R2</sup>

We chose an optimum mixture consisting of 1.5 wt.% thiophene and 2.3 wt.% ferrocene to study the elemental distribution of C, S and Fe atoms

into their corresponding species from 100 °C up to the flame temperature of 1471 °C at  $\phi = 1.05$  (7.0 slpm H<sub>2</sub> and 16.7 slpm air). The results were then compared to that without sulphur, *i.e.* 0 wt.% thiophene and 2.3 wt.% ferrocene at  $\phi = 1.05$ . The results are graphed in the following sections to reflect the species/phase transition of a specific element as temperature increases.

The methodology of the numerical analysis is as follows. First, the experimental parameters, including the reactant species, mass fluxes and the burner temperatures, for the CNT synthesis serve as the key inputs for the computational study. The 1-D flame simulations use these experimental results to calculate the flame temperatures and the post-flame products, which are the input parameters for the following 2-D diffusion model. The spatially resolved distribution of mass fractions of the reactants and the surrounding and the local temperatures estimated by the 2-D model are then used for the thermodynamic equilibrium calculations. Finally, a spatially-resolved distribution of equilibrium species resolves the species considered for a full picture of the entire process from a thermodynamic perspective.

## 4. Experimental Results

### 4.1. Effect of ferrocene

Figure 2 shows the average normalised Raman spectra of the nanomaterials produced using different mass proportions of ferrocene  $y_{Fe}$  at  $\phi = 1.05$ . A sharp and distinct G-band at 1590 cm<sup>-1</sup>, D-band at 1330 cm<sup>-1</sup> and the radial breathing mode (RBM) feature at lower wave numbers (< 300 cm<sup>-1</sup>) for different  $y_{Fe}$  considered. The peak at 670 cm<sup>-1</sup> appearing on all the

Raman spectra is believed to be that of magnetite  $\text{Fe}_3\text{O}_4$  [67, 68]. Yet the variation of this peak shows no positive correlation with  $y_{\text{Fe}}$ . Further, the changing  $y_{\text{Fe}}$  does not appear to ~~affected~~ affect the intensity ratio of G-band to D-band,  $I_G/I_D$ , an indicator of CNT quality or purity [69]. The ratio  $I_G/I_D$  peaks when the mass fraction of the ferrocene in the central tube feedstock  $y_{\text{Fe}}$  equals to 3.0% in contrast to the lowest at  $y_{\text{Fe}} = 2.0\%$ . Similar results are obtained at higher  $\phi$ . As  $\phi$  increases from 1.05 to 1.2, an increase in background noise in the Raman spectra and fading CNT Raman features including a drop in  $I_G/I_D$ , an increase in the magnetite peak and vanishing RBM band are clearly observed for all  $y_{\text{Fe}}$ . This indicates that the CNT number density has a much higher temperature dependence over the concentration of ferrocene. Accordingly, the results suggest that with the addition of ferrocene, CNTs can be successfully synthesised over a range of  $y_{\text{Fe}}$ , but higher number density and better quality of CNTs can only achieved at higher temperatures above 1300 °C, as suggested by the theoretical estimations [44]. As  $\phi$  increases from 1.05 to 1.2, a decreased yield of CNTs is evidenced by the increase in noise arising the Raman spectra, accompanied by the fading CNT Raman features for all  $y_{\text{Fe}}$ . A drop in  $I_G/I_D$ , an increase in the magnetite peak and the vanishing RBM band are observed. The results show that with the addition of ferrocene, CNTs can be successfully synthesised over a range of  $y_{\text{Fe}}$ , but higher yields and higher quality as defined by the G/D ratio are obtained at higher temperatures above 1300 °C, as suggested by the theoretical estimations [44].<sup>R2</sup> This temperature range is consistent with the results reported by floating catalyst CVD studies where 1150–1450 °C, and seems to be ideal for SWCNT formation [40].

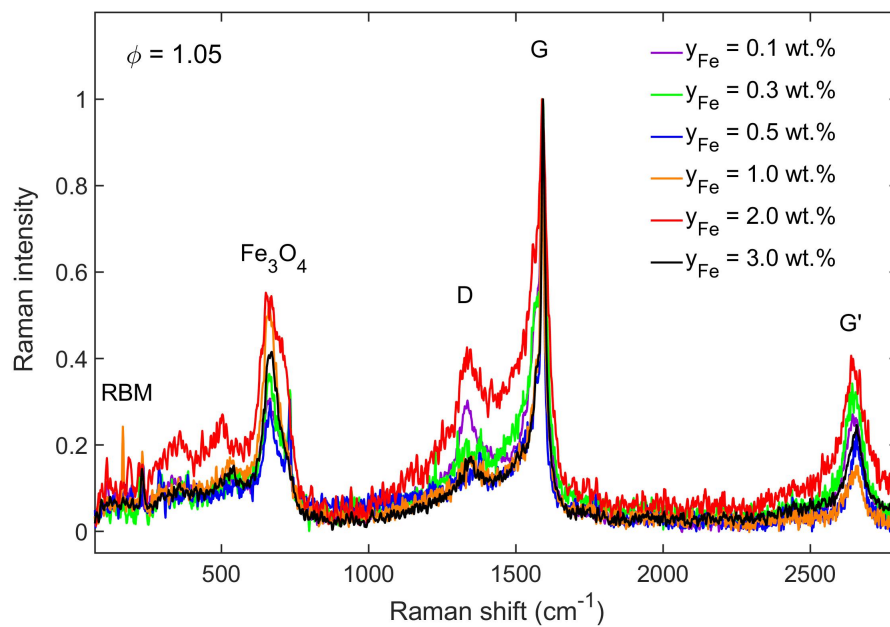


Figure 2: Average normalised Raman spectra of the samples produced using reactant mixtures with different mass fractions of ferrocene  $y_{Fe}$  at different  $\phi$  of 1.05.

SEM analyses were performed to examine the as-produced materials at the nanoscale. Figure 3 shows the morphology of the samples produced at  $\phi = 1.05$  over different  $y_{Fe}$  where a web-like scaffolding structure prevails. Direct measurements on the images suggest that the diameter of individual CNTs or CNT bundles synthesised at different  $y_{Fe}$  are of the order of 10 nm, and their lengths can vary from 10 nm up to 1  $\mu\text{m}$ . By comparison, the variation of  $y_{Fe}$  appears to have little impact on the morphology of the CNT products, and no marked changes of the number density of CNTs against nanoparticles are observed. Yet there is a positive correlation between  $y_{Fe}$  and the overall yield of solid products including nanoparticles and CNTs, as these solids are seen more closely packed at higher  $y_{Fe}$  due to the increased amount of iron input with increasing  $y_{Fe}$ . The results reveal that the CNT synthesis is insensitive to the variation of  $y_{Fe}$  so long as there exists an iron precursor. The iron precursor then decomposes into catalytically active nanoparticles on which CNTs start to form and grow given at a suitable temperature. The remaining fraction of iron atoms, in a relatively larger quantity, preferably combine with oxygen to form iron oxides due to the presence of  $\text{H}_2\text{O}$ . The morphology of samples produced with varying  $\phi$  for different  $y_{Fe}$  were also examined by SEM. In general, the evolution of the sample morphology as  $\phi$  varies from 1.05 to 1.2 closely resemble our previous findings: the web-like scaffolding structure is replaced with by aggregates of nanoparticles with few CNTs observed in the analysis [44]. The SEM results combined with the previous Raman spectroscopy further reveal the dominating role of temperature on the yield and quality of CNTs produced in the process in contrast to a weaker effect by the variation of ferrocene

concentrations.<sup>R2</sup>

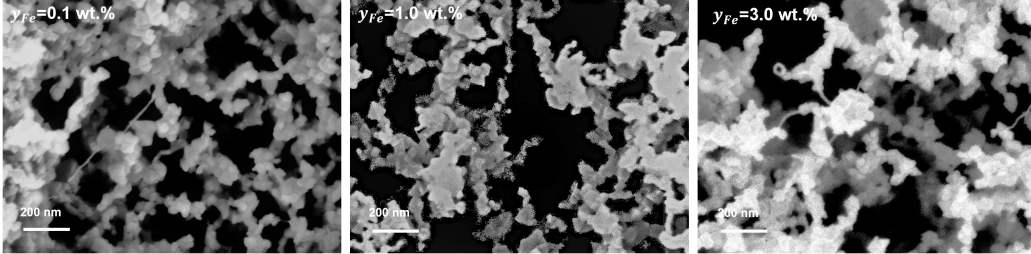


Figure 3: SEM images of samples produced at  $\phi = 1.05$  using feedstocks of different mass fractions of ferrocene  $y_{Fe}$ .

#### 4.2. Effect of sulphur catalyst

Figure 4 demonstrates the average normalised Raman spectra for samples synthesised at  $\phi$  from 1.05 to 1.20 using reactants in a range of sulphur-to-iron mass ratios,  $m_{S/Fe}$ , from 0 to 10.1, corresponding to the conditions of Test 4 and 7-11 (see Table 1), respectively. According to Fig.4, the effect of sulphur on the production becomes manifest even at very low sulphur levels. Although the Raman spectra at various  $m_{S/Fe}$  appear alike at  $\phi = 1.05$  showing distinct CNT features, those with sulphur show a differentiated pattern compared to that without: a comparable  $I_G/I_D$  ratio at around 3.5, an intensified RBM and second order G'-band, and a lowered peak associated with magnetite  $Fe_3O_4$  at  $670\text{ cm}^{-1}$ .

As the ratio of mass between thiophene and ferrocene in the central tube feedstock  $m_{S/Fe}$  increases, those cases with zero sulphur ( $m_{S/Fe} = 0$ ) are more sensitive to the change of temperature compared with those with sulphur, which is evidenced by the variation of  $I_G/I_D$  as indicated in Fig. 5. From the figure,  $I_G/I_D$  for  $m_{S/Fe} = 0$  decreases strongly from 7.7 down to 2.2

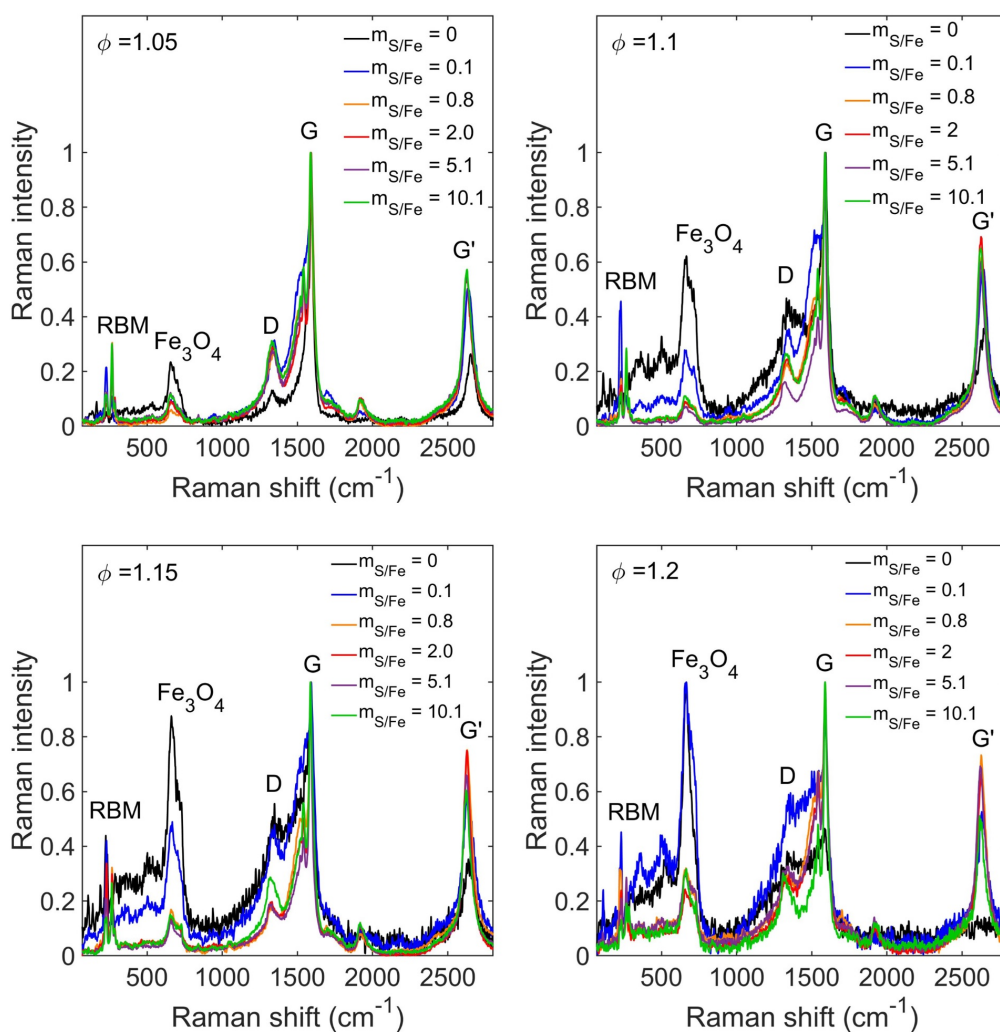


Figure 4: Average normalised Raman spectra of the samples produced using feedstock with varying mass ratios of sulphur to iron  $m_{S/Fe}$  from 0. to 10.1 at different  $\phi$  of (a) 1.05, (b) 1.10, (c) 1.15 and (d) 1.20.

as  $\phi$  increases from 1.05 to 1.10. In contrast, for cases at  $m_{S/Fe} > 0$  the addition of sulphur appears to help retain the CNT Raman features of the samples against the decreasing temperature as  $\phi$  increases, particularly for those with higher  $m_{S/Fe}$ . Specifically, it shows that  $I_G/I_D$  for  $m_{S/Fe} = 0.1$  only drops slightly from 3.2 to 2.8 as  $\phi$  increases from 1.05 to 1.10, indicating an enhanced resistance to the drop of temperatures compared to the case without sulphur. Moreover, in contrast to a monotonic decrease in the cases of  $m_{S/Fe} \leq 0.1$ , an increase in  $I_G/I_D$  over increasing  $\phi$  is seen, in particular for  $m_{S/Fe} = 5.1$  where  $I_G/I_D$  rises over 70% from 3.6 to 6.2 as  $\phi$  increases to 1.10. As  $\phi$  reaches 1.20, CNT features disappear for the zero sulphur case. But for sulphur cases, the products' Raman spectra highly resemble those at  $\phi = 1.05$ , including  $I_G/I_D$ , albeit slightly higher signal-to-noise ratios and an enhanced intensity of magnetite. The role of sulphur, as the results imply, seems to partly offset the adverse effect of lower temperatures due to increasing  $\phi$ , which lowers the minimum threshold temperature required for the inception and growth of CNTs.

To further understand the changes of the Raman spectra of CNTs as a result of sulphur addition, the Raman spectra near the region between the D and G bands, 1200–1650  $\text{cm}^{-1}$ , are deconvoluted into 4 Lorentzian peaks, D, D3, G<sup>-</sup> and G<sup>+</sup> modes using the Gaussian-Lorentzian fitting function [70], for the cases at  $\phi = 1.05$  as illustrated in Fig.6. Due to the high similarity in the Raman spectra, the spectrum for  $m_{S/Fe} = 0.8$  is chosen to represent those of higher  $m_{S/Fe}$ . The shaded dots illustrate the original data while the thick black line and the thin lines in various colours represent the fitting curve and the deconvoluted peaks, respectively. Clearly observed in

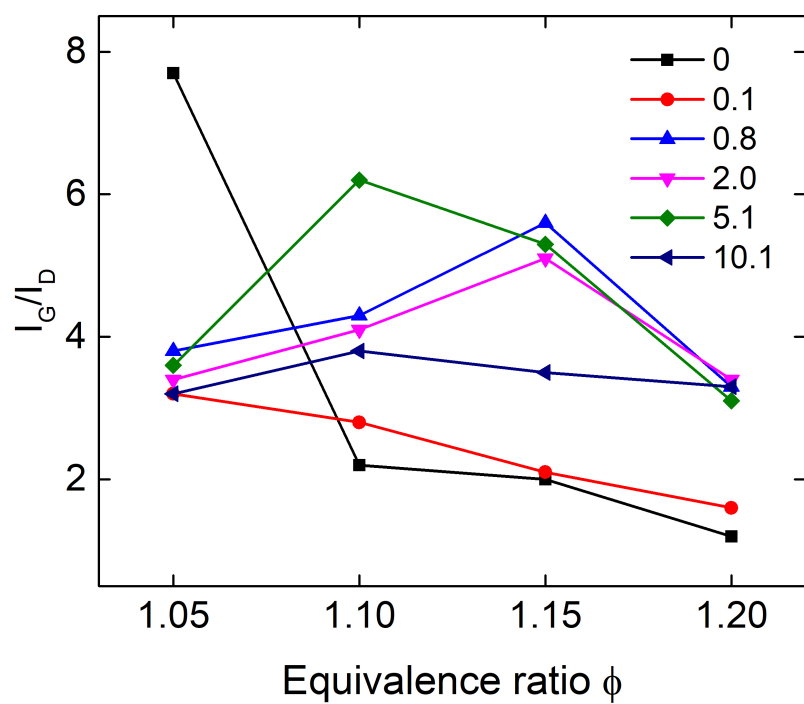


Figure 5: Average normalised Raman intensity ratios of the G-band to D-band  $I_G/I_D$  as a function of equivalence ratios  $\phi$  from 1.05 to 1.20 for the samples produced using the feedstocks of different sulphur-to-iron mass ratios  $m_{S/Fe}$  from 0 to 10.1.

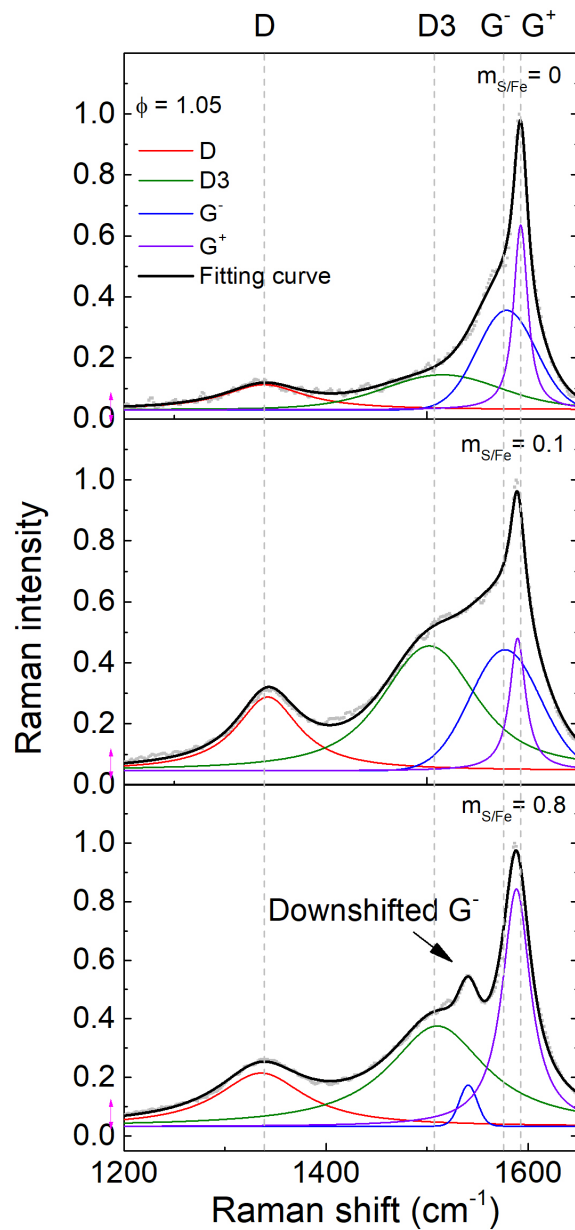


Figure 6: Normalised Raman spectra (shaded dot) and their spectral deconvolution into Lorentzian peaks in the range of wave number between 1200 and 1650  $\text{cm}^{-1}$  for the samples produced with different sulphur-to-iron mass ratios  $m_{S/Fe}$  from 0 to 0.8 at  $\phi = 1.05$ .

Fig.6 is the marked transition of the Raman spectra as  $m_{S/Fe}$  increases. A broadening effect is seen at the G-band, in particular at lower frequencies, owing to the increased intensity of D and D3 peaks after the addition of sulphur. Specifically, the relative intensity ratio between D and D3 peaks is hardly affected by the sulphur catalyst, merely rising from 1.3 to 1.6 as  $m_{S/Fe}$  increases from 0 to 0.8. Rather, their normalised intensities are tripled and doubled at  $m_{S/Fe} = 0.1$  and 0.8, respectively. The D peak, a common feature present in carbon allotropes, is associated with defects in materials, whereas the D3 peak is mostly observed in amorphous carbon, in particular soot [70]. Apart from the broadening line shape of the G-band, downshift of the  $G^+$  and  $G^-$  peaks are also observed for all the samples with  $m_{S/Fe} \geq 0.1$  regardless of the variation of  $\phi$ . Such characteristic feature in the G-band appears to be consistent with those found in metallic CNTs, under a specific name of Breit-Wigner-Fano lineshape [69, 71]. The phenomena of an enhanced intensity of the RBM and  $G'$ -band, and downshifted and lowered G-band features have also been observed by experimental and numerical studies in isolated metallic SWCNTs comparing with the semiconducting counterparts [69, 71, 72]. Hence, the present experimental results may imply that adding sulphur to the synthesis would contribute to a transition from semiconducting to metallic chirality.

XRD analysis was applied to investigate the identity of the crystalline nanoparticles. Illustrated in Fig.7 are the XRD patterns of  $Fe_3O_4$ , PTFE substrate and the synthesis materials produced at  $\phi = 1.05$ . The results, together with the featured Raman peak at around  $670\text{ cm}^{-1}$  shown in Fig.4, confirm the crystalline nanoparticles are primarily  $Fe_3O_4$ , to which the CNT

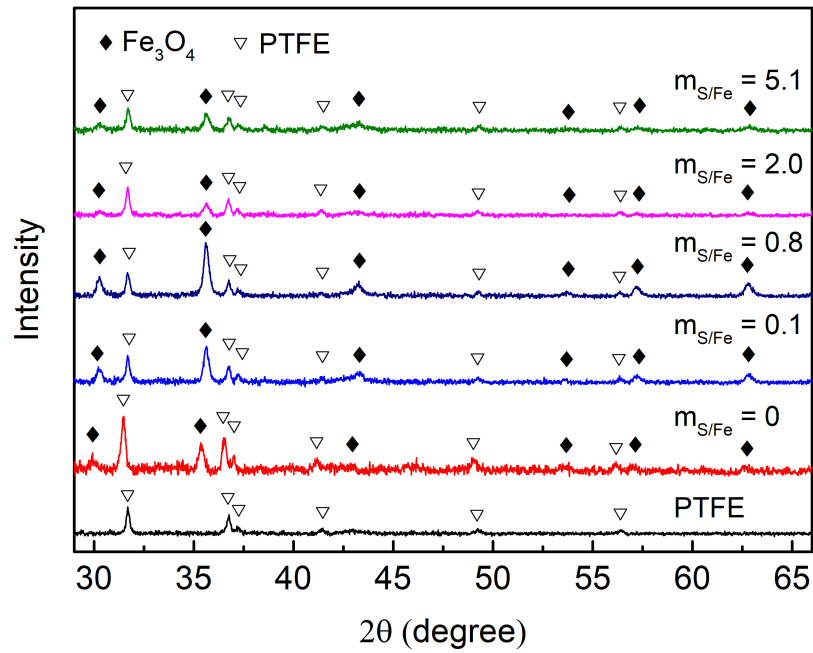


Figure 7: XRD pattern of PTFE substrate and the samples produced at  $\phi = 1.05$  using the feedstock with different sulphur-to-iron mass ratios  $m_{\text{S/Fe}}$  from 0 to 5.1.

fibres are attached.

Figure 8.(a)-(c) compares the SEM images of samples produced at  $\phi = 1.05$  with  $m_{S/Fe}$  of 0.1, 0.8 and 10.1. By comparing the SEM images in Fig.3, the addition of sulphur induces a marked change in the morphology, even given a very small amount (0.1 wt.% of thiophene in the feedstock). Isolated CNT fibres and their webs are more clearly seen on the samples with sulphur, showing an increased number density of CNTs despite the presence of nanoparticles. Moreover, CNTs formed with sulphur are produced in a much larger quantity and longer lengths in contrast to those formed without sulphur. The diameter of CNTs or CNT bundles (see the insert of Fig.8.(b)) formed can vary but are below 10 nm, comparable to those at  $m_{S/Fe} = 0$ . As  $m_{S/Fe}$  increase beyond 0.8, the improvement of the number density of CNTs ceases, and the morphology starts to transit into a closely packed clumps embedding CNT fibres beneath from a cotton-like morphology as demonstrated in Fig.8.(c).

As indicated in Fig.4, the CNT Raman features still remain pronounced as  $\phi$  increases, indicating that, in contrast to the cases without sulphur, the production of CNTs is less affected by the increase of  $\phi$  or lower flame temperatures, when sulphur added. This suggests an extended lower limit of synthesis temperature and hence an enlarged formation window as a result of sulphur. Hence we examined the samples produced at higher  $\phi$  using SEM. Figure.8.(d)-(f) summarise the transition of morphology of samples produced at  $\phi = 1.20$  with increasing  $m_{S/Fe}$  from 0 to 5.1. For  $m_{S/Fe}=0$ , CNTs are neither found by SEM nor by Raman spectroscopy, indicating the absence of CNTs. Rather, closed-packed crystalline magnetite of around 50

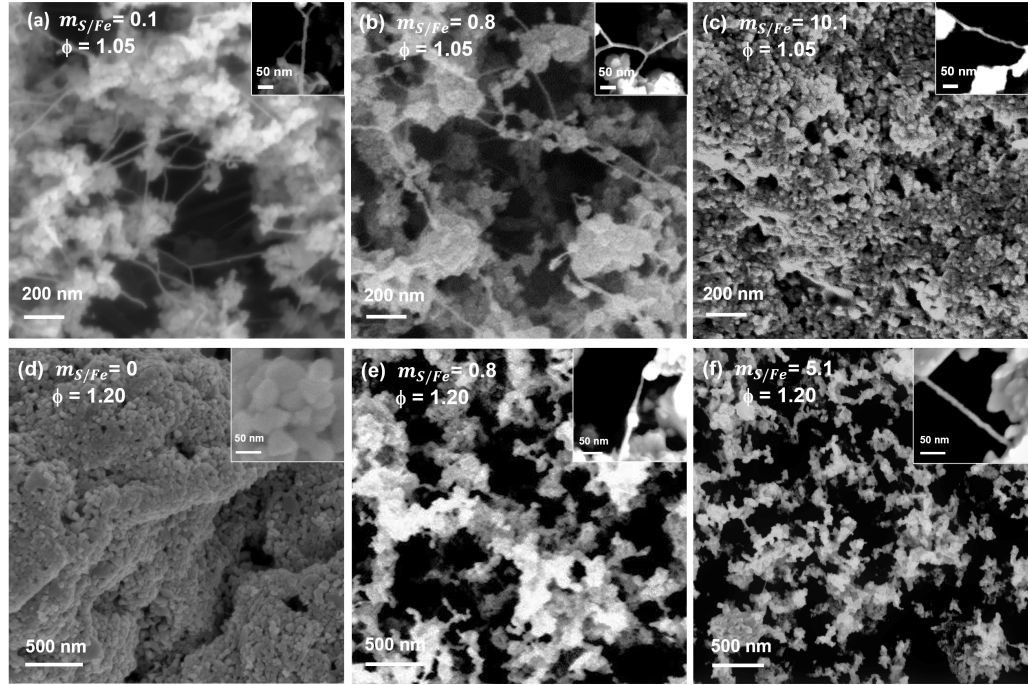


Figure 8: SEM images of the samples produced at  $\phi = 1.05$  using the feedstock with  $m_{S/Fe}$  of (a) 0.1, (b) 0.8 and (c) 10.1, and at  $\phi = 1.20$  with  $m_{S/Fe}$  of (d) 0, (e) 0.8 and (f) 5.1.

nm prevail in the image (Fig.8.(d)). When sulphur added to the synthesis, the morphology of the products significantly changes. From Fig.8.(e) and (f), the morphology of both cases closely resembles regardless of different  $m_{S/Fe}$ , showing a weakened impact by the variation of sulphur concentration as synthesis temperature decreases. These two samples both exhibit the cotton-like structure with shorter CNTs compared to those at lower  $\phi$  connecting crystalline nanoparticles similar to Fig.3. This provides the direct evidence that adding sulphur extends the lower limit of synthesis temperature. It is possible to examine the lengths of the SWCNTs produced in of six cases showed in Fig.8 (a) to (f) via direct measurements in the SEM images.

However, SWCNTs are bounded together, and the spatial orientations of the bundles are varied, preventing the accurate determination of length. Future work may be done on using dissolution techniques to separate the CNTs for such measurements, which were beyond the current study.<sup>R2</sup>

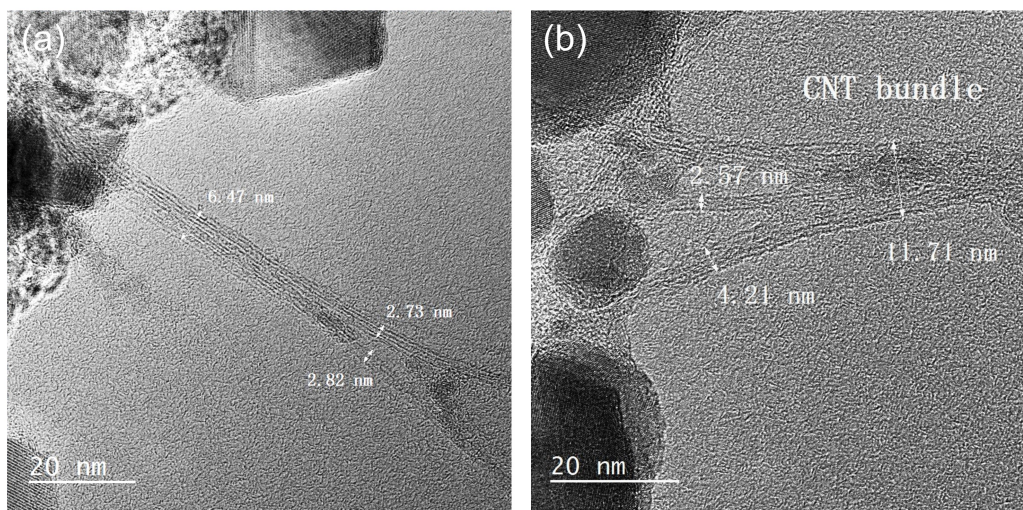


Figure 9: TEM images of the samples produced at  $\phi = 1.05$  using the feedstock with the sulphur-to-iron mass ratio  $m_{S/Fe}$  of 1.2 (2.0 wt.% of ferrocene and 1.9 wt.% of thiophene).

TEM images of the samples with  $m_{S/Fe} = 1.2$  produced at  $\phi = 1.05$  in Fig. 9 confirm the existence of SWCNTs as the hollow cylindrical structures are clearly seen. Figure 9(a) depicts a splitting CNT bundle originated from the nanoparticles on the upper-left of the image. This CNT bundle has an outer diameter of 6.5 nm, consisting of individual single-walled CNTs of around 1 nm in diameter. The CNT bundle splits into 2 or 3 smaller CNT bundles as it grows away from the nanoparticles. Figure 9 (b) provides a closer look at the roots of a CNT bundle. It is seen that most of the nanoparticles are highly crystallised, possessing well-ordered arrangements

of atoms or molecules. These ordered structures are either iron oxides or elemental iron solids, which are covered by multiple layers of amorphous carbon.

## 5. Discussion

The characterisation of the as-produced materials from the flame synthesis provides insight into the process of flame synthesis. According to Raman spectroscopy, XRD, SEM and TEM analysis, CNT bundles of individual nanotubes of diameter around 1 nm are produced along with vast amounts of crystalline nanoparticles that are identified as iron oxides, primarily magnetite  $\text{Fe}_3\text{O}_4$ . The quality of CNTs in terms of length and diameter shows insensitivity to the change of the ferrocene input, while the number density of the iron oxide nanoparticles exhibit positive correlation with the ferrocene concentration. Sulphur is identified as an effective promoter for CNT synthesis as the CNTs produced with sulphur exhibit a longer length and a better number density compared to those without sulphur. Furthermore, the experiments suggest that the addition of sulphur extends the lower limit of threshold temperature required for CNT growth, *i.e.* CNTs can form at a lower temperature which extends the growth phase for CNTs if sulphur is present. To gain further understanding of the effect of catalysts on the CNT production, additional 2-D simulations of the expected mixture fraction and temperature have been performed, and the results are shown in Fig. 10.

Results illustrated in Fig. 10, from left to right, are the spatial distribution of mixture fraction  $\xi$ , local temperature  $T$ , and the image of the synthesis region, respectively. The reactants, representing ethanol and argon, injected

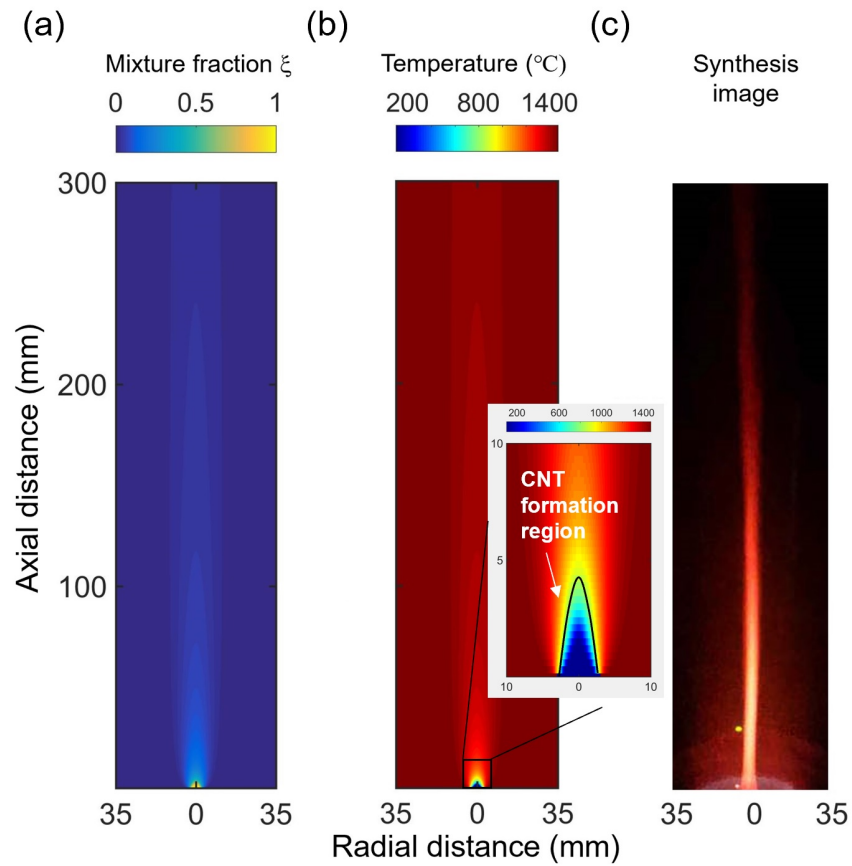


Figure 10: Simulated results for the axisymmetric pyrolysis zone under combustion synthesis. The outer mixture is calculated at  $\phi = 1.05$  (7.0 slpm  $H_2$  and 16.7 slpm air) and the central ethanol stream is injected at  $0.5 \text{ mL/minml/min}^{R3}$  and carried by an argon stream at 0.1 slpm. Rightmost image shows a photograph of the flame under pyrolysis condition.

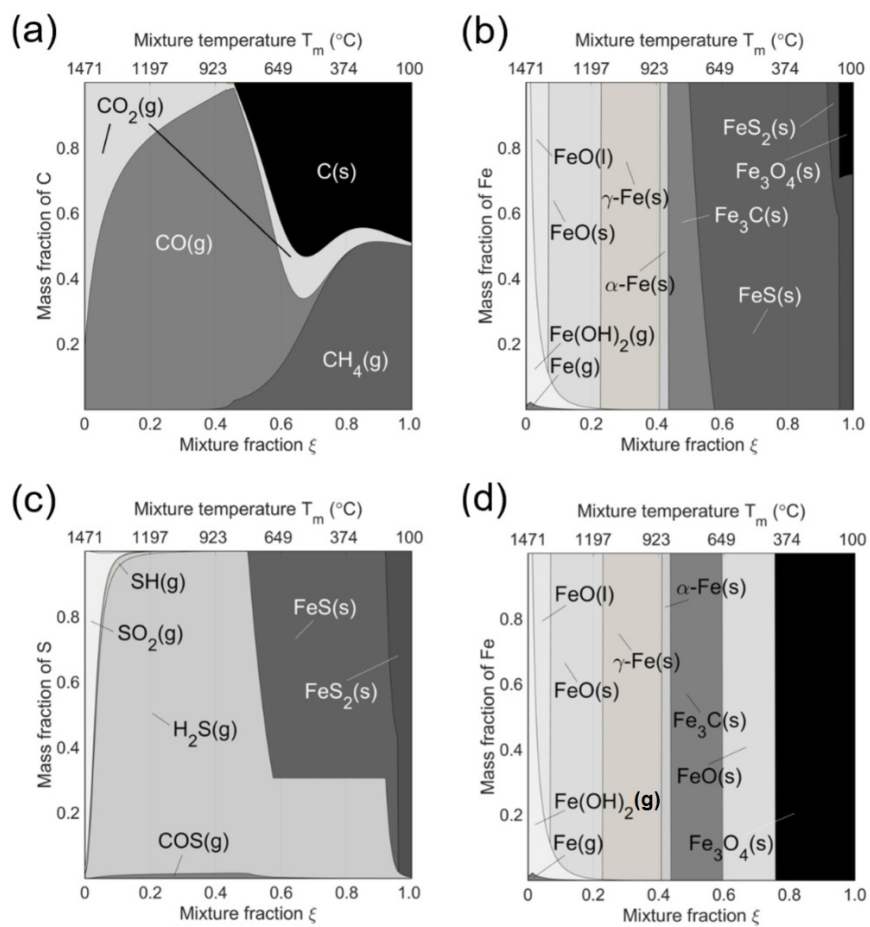


Figure 11: (a)-(c) Thermodynamic equilibrium transitions of C, Fe and S atoms from  $\xi$  of 0 to 1.0 at  $\phi = 1.05$  (7.0 slpm  $\text{H}_2$  and 16.7 slpm air) with the ethanol feedstock of 1.5 wt.% thiophene and 2.3 wt.% ferrocene. (d) Thermodynamic equilibrium transition of Fe atoms at  $\phi = 1.05$  (7.0 slpm  $\text{H}_2$  and 16.7 slpm air) with the ethanol feedstock with no sulphur (2.3 wt.% ferrocene only).

from the central tube that has  $\xi = 1$ , diffuse out quickly with increasing axial distance, and the temperature by definition shows the opposite behaviour, since they are connected using reaction [50]. The temperature at  $r = 0$  rapidly increases to 1000 °C at just 6 mm in the axial direction, quickly reaching the threshold temperature suitable for making SWCNTs suggested by floating catalyst CVD studies [13, 31, 73]. Figure 10(c) shows the actual synthesis region where the reddish glow is likely due to the luminescence from the heated iron oxide nanoparticles.

Mass fractions and temperature distributions can be calculated using the 2-D model, from which the equilibrium species can be calculated as shown on Fig. 11. In this figure, we note that a linear function connects the mixture temperature and mixture fraction, as depicted in the top and bottom scales of each subplot. Zero mixture fraction corresponds to pure hot burned gases, and unity mixture fraction, the pure incoming reactant stream.

Figure 11 shows how the elements C, S and Fe are partitioned at equilibrium according to the expected temperatures and mixture fractions found in the 2-D simulations. Figure 11(a) shows how conversion of ethanol to solid carbon C(s) becomes possible for mixture fractions of 1.0 to 0.46046 and 1.0<sup>R3</sup>, corresponding to the temperature range of 100 to 841 °C, respectively. For higher temperatures and lower mixture fractions, the ratio of carbon to the surrounding oxygen is insufficient for conversion in spite of the higher temperatures, and equilibrium favours the formation of oxygenated species CO<sub>2</sub> and CO. One must keep in mind of course that equilibrium is a limit case, and that the conversion is likely kinetically limited by temperatures available. The addition of sulphur was not found to significant affect the

distribution of carbon, and it is the same as in Fig. 11(a).

The partition of S itself as shown in Fig.11(c) as a function of  $\xi$ . The pure reactant mixture and down to  $\xi \geq 0.5$  converts to solid iron sulphides, FeS(s) and FeS<sub>2</sub>(s), corresponding to temperature below 786 °C. At lower  $\xi$  towards higher temperatures, all S atoms are at equilibrium converted primarily to H<sub>2</sub>S.

Fig.11.(b) and (d) compares the partition of iron atoms for the case with sulphur to that without, respectively. Major differences are found at  $\xi \geq 0.5$ , which overlaps the region for C(s) formation. For the case with sulphur, iron oxides and iron sulphides both form at high  $\xi$  or low temperatures, in the form of Fe<sub>3</sub>O<sub>4</sub>(s) and FeS<sub>2</sub>(s). As  $\xi$  decreases, or temperature increases, solid iron sulphides, primarily FeS(s), become the dominant iron-containing species up to around 0.58 where solid iron carbides, Fe<sub>3</sub>C(s) forms. As  $\xi$  decreases from 0.58 to 0.5, Fe<sub>3</sub>C(s) and FeS(s) are seen to coexist in that range, corresponding to 676 to 786 °C, respectively. In comparison, for the no sulphur case (see Fig.11(d), iron oxides dominate the iron species at  $\xi \geq 0.6$ : FeO prevails at  $\xi$  between 0.6 and 0.76 and Fe<sub>3</sub>O<sub>4</sub> at  $\xi \geq 0.76$ . As  $\xi$  decreases, Fe<sub>3</sub>C(s) exist between 0.43 and 0.6, corresponding to 882 and 659 °C, respectively. From  $\xi \leq 0.42$ , both cases exhibit the same species distribution where iron transits from solid iron where iron transits from iron transits from solid iron<sup>R3</sup>  $\alpha$ -Fe(s) to  $\gamma$ -Fe(s) up to  $\xi = 0.23$ . As  $\xi$  decreases further, iron is oxidised again to form FeO in solid and gas phases, along with the formation of gas phase iron and Fe(OH)<sub>2</sub>(g).

By comparing the two cases, the roles of sulphur become clearer from the perspective of thermodynamic equilibrium. First, it prevents iron from oxi-

dation at lower temperatures by binding iron into iron sulphides, which likely preserves the activity of iron nanoparticles for the following CNT formation, as this "poisoning" effect [74] is usually reversible [42]. Second, the coexistent region for FeS(s) and Fe<sub>3</sub>C(s) and the "delayed" formation of Fe<sub>3</sub>C(s) due to the presence of sulphur suggest that the formation of iron carbides is moderated by sulphur as temperature changes. This process might reserve the activity of iron from being deactivated by layered carbon or iron carbides as suggested in [40]. Further, the equilibrium results provides the hint for the locations suitable for CNT formation. By referring the formation window of  $\xi$  for solid carbon C(s), iron sulphides and iron carbides, the possible region for CNTs and catalyst nanoparticles formation is bounded by an envelope of  $\xi$  between 1.0 to ~~0.46046~~ and ~~1.0~~<sup>R3</sup>, corresponding to the temperature range of 841 to 100 °C, indicated in the insert in Fig.10.(b). Such finding explains the reason why the overall length of the SWCNTs produced by the present method is markedly shorter than those by CVD methods as limited formation region and short residence time significantly limits the growth of CNTs.

## 6. Conclusions

We systematically investigated the effects of ferrocene and thiophene on the CNT synthesis using a floating catalyst combustion system where pre-mixed H<sub>2</sub>/air flames at different  $\phi$  from 1.05 to 1.2 were used as the heat source. Different characterisation techniques were used to determine the properties of the as-produced materials including Raman spectroscopy, scanning electron microscopy, and transmission electron microscopy. SWCNTs

and crystalline magnetite were identified as the primary products. The sensitivity of the as-produced products to the feedstock of varying sulphur to iron mass ratios from 0 up to 10.1 were tested. Ferrocene was found to have little influence on regulating the proportions of CNTs over nanoparticles but rather to slightly increase the overall yield of both. The experiments revealed that sulphur has an effect of moderating the proportion of CNTs over nanoparticles, with higher levels favouring the formation of CNTs, with an optimum range of  $m_{S/Fe}$  was identified as 0.1–2. Furthermore, by adding sulphur, the quantity and length of the CNTs were much larger compared to those without sulphur, in particular at  $\phi = 1.05$  corresponding to a computed flame temperature of  $\sim 1451$  °C. In addition, sulphur also appears to lower the minimum threshold temperature for the formation of CNTs.

We constructed a set of simple linked diffusion-equilibrium models to study the mechanisms of the synthesis. As suggested by thermodynamic equilibrium, the "poisoning" effect of sulphur likely preserves the activity of iron nanoparticles by reversible binding of iron into iron sulphides (FeS and FeS<sub>2</sub>), which prevents iron from being oxidised at lower temperatures. Further, the formation of iron carbides is moderated by sulphur as temperature changes, which might help reduce the amount of layered carbon or iron carbides that encapsulate iron nanoparticles. The local region ( $< 5mm$  in axial direction) and temperatures (100–841 °C) suitable for CNT formation are also identified by virtue of modelling. The theoretical analysis indicates that the limited formation region and short residence time significantly constrain the formation and growth of CNTs.

## Acknowledgements

Cen Zhang thanks the China Scholarship Council and the Cambridge Trust for the financial support towards this research work. The overall project is funded under EPSRC UK Award EP/M015211/1 for the ANAM Initiative. The authors thank Dr Xiao Zhang and Dr Yanting Jin for their help with Raman and XRD analysis. The authors are also grateful to Dr Adam Boies and Prof Alan Windle for helpful discussions.

## References

- [1] E. T. Thostenson, Z. Ren, T.-W. Chou, *Composites Science and Technology* 61 (2001) 1899–1912.
- [2] B. Marinho, M. Ghislandi, E. Tkalya, C. E. Koning, G. de With, *Powder Technology* 221 (2012) 351–358.
- [3] J. Hone, M. C. Llaguno, M. J. Biercuk, a. T. Johnson, B. Batlogg, Z. Benes, J. E. Fischer, *Applied Physics A: Materials Science & Processing* 74 (2002) 339–343.
- [4] R. H. Baughman, Z. Anvar A., W. A. de Heer, *Science* 297 (2002) 787.
- [5] M. F. L. D. Volder, S. H. Tawfick, R. H. Baughman, A. Hart, *Science* 535 (2013) 535–540.
- [6] R. Mora, J. Vilatela, A. Windle, *Composites Science and Technology* 69 (2009) 1558–1563.
- [7] J. Suhr, N. Koratkar, P. Keblinski, P. Ajayan, *Nature Materials* 4 (2005) 134–137.

- [8] G. Lota, K. Fic, E. Frackowiak, *Energy and Environmental Science* 4 (2011) 1592–1605.
- [9] A. Beigbeder, P. Degee, S. L. Conlan, R. J. Mutton, A. S. Clare, M. E. Pettitt, M. E. Callow, J. A. Callow, P. Dubois, *Biofouling* 24 (2008) 291–302.
- [10] Z. Wu, Z. Chen, X. Du, J. M. Logan, J. Sippel, M. Nikolou, K. Kamaras, J. R. Reynolds, D. B. Tanner, A. F. Hebard, A. G. Rinzler, *Science* 305 (2004) 1–3.
- [11] H. Shirae, K. Hasegawa, H. Sugime, E. Yi, R. M. Laine, S. Noda, *Carbon* 114 (2017) 31–38.
- [12] J.-F. Colomer, C. Stephan, S. Lefrant, G. Van Tendeloo, I. Willems, Z. Kónya, A. Fonseca, C. Laurent, J. Nagy, *Chemical Physics Letters* 317 (2000) 83–89.
- [13] Y.-L. Li, I. A. Kinloch, A. H. Windle, *Science (New York, N.Y.)* 304 (2004) 276–8.
- [14] F. Danafar, A. Fakhru'l-Razi, M. A. M. Salleh, D. R. A. Biak, *Chemical Engineering Journal* 155 (2009) 37–48.
- [15] W. Merchan-Merchan, A. V. Saveliev, L. Kennedy, W. C. Jimenez, *Progress in Energy and Combustion Science* 36 (2010) 696–727.
- [16] R. Sen, Y. Ohtsuka, T. Ishigaki, D. Kasuya, S. Suzuki, H. Kataura, Y. Achiba, *Chemical Physics Letters* 332 (2000) 467–473.

- [17] N. Arora, N. N. Sharma, *Diamond and Related Materials* 50 (2014) 135–150.
- [18] W. Y. Teoh, R. Amal, L. Mädler, *Nanoscale* 2 (2010) 1324–1347.
- [19] J. Howard, K. Chowdhury, J. Sande, *Nature* 370 (1994) 603.
- [20] R. L. Vander Wal, L. J. Hall, G. M. Berger, *The Journal of Physical Chemistry B* 106 (2002) 13122–13132.
- [21] L. Yuan, K. Saito, C. Pan, F. Williams, A. Gordon, *Chemical Physics Letters* 340 (2001) 237–241.
- [22] W. Merchan-Merchan, A. Saveliev, *Chemical Physics Letters* 354 (2002) 20–24.
- [23] M. D. Diener, N. Nicholson, J. M. Alford, *The Journal of Physical Chemistry B* 104 (2000) 9615–9620.
- [24] R. L. Vander Wal, L. J. Hall, G. M. Berger, *Proceedings of the Combustion Institute* 29 (2002) 1079–1085.
- [25] R. V. Wal, L. Hall, *Chemical Physics Letters* 349 (2001) 178–184.
- [26] R. Vander Wal, *Carbon* 40 (2002) 2101–2107.
- [27] M. J. Height, J. B. Howard, J. W. Tester, J. B. Vander Sande, *Carbon* 42 (2004) 2295–2307.
- [28] J. Z. Wen, H. Richter, W. H. Green, J. B. Howard, M. Treska, P. M. Jardim, J. B. Vander Sande, *Journal of Materials Chemistry* 18 (2008) 1561–1569.

- [29] R. L. Vander Wal, T. M. Ticich, *The Journal of Physical Chemistry B* 105 (2001) 10249–10256.
- [30] C. T. Chong, W. H. Tan, S. L. Lee, W. W. F. Chong, S. S. Lam, A. Valera-Medina, *Materials Chemistry and Physics* 197 (2017) 246–255.
- [31] Y.-L. Li, L.-H. Zhang, X.-H. Zhong, A. H. Windle, *Nanotechnology* 18 (2007) 225604.
- [32] S. Chaisitsak, J. Nukeaw, A. Tuantranont, *Diamond and Related Materials* 16 (2007) 1958–1966.
- [33] R. Andrews, D. Jacques, A. Rao, J. Chen, *Chemical physics Letters* 303 (1999) 467–474.
- [34] H. W. Zhu, C. L. Xu, D. H. Wu, B. Q. Wei, R. Vajtai<sup>2</sup>, P. M. Ajayan, *Science* 296 (2002) 884–886.
- [35] G. H. Du, W. Z. Li, Y. Q. Liu, Y. Ding, Z. L. Wang, *Journal of Physical Chemistry C* 111 (2007) 14293–14298.
- [36] R. M. Sundaram, K. K. K. Koziol, A. H. Windle, *Advanced Materials* 23 (2011) 5064–5068.
- [37] C. Hoecker, F. Smail, M. Pick, A. Boies, *Chemical Engineering Journal* 314 (2017) 388–395.
- [38] G. G. Tibbetts, C. A. Bernardo, D. W. Gorkiewicz, R. L. Alig, *Carbon* 32 (1994) 569–576.

- [39] G. G. Tibbetts, M. P. Balogh, *Carbon* 37 (1999) 241–247.
- [40] M. S. Motta, A. Moisala, I. A. Kinloch, A. H. Windle, *Journal of Nanoscience and Nanotechnology* 8 (2008) 2442–2449.
- [41] M. Motta, Y. L. Li, I. a. Kinloch, a. H. Windle, *Nano Letters* 5 (2005) 1529–1533.
- [42] Y. Yuan, L. Wei, W. Jiang, K. Goh, R. Jiang, R. Lau, Y. Chen, *Journal of Materials Chemistry A* 3 (2015) 3310–3319.
- [43] S. Okada, H. Sugime, K. Hasegawa, T. Osawa, S. Kataoka, H. Sugiura, S. Noda, *Carbon* 138 (2018) 1–7.
- [44] C. Zhang, B. Tian, C. T. Chong, B. Ding, L. Fan, X. Chang, S. Hochgreb, *Materials Chemistry and Physics* 254 (2020) 123479.
- [45] *Proceedings of the National Academy of Sciences of the United States of America* 102 (2005) 16141–5.
- [46] J. B. In, C. P. Grigoropoulos, A. A. Chernov, A. Noy, *ACS nano* 5 (2011) 9602–9610.
- [47] G. P. Smith, D. M. Golden, M. Frenklach, N. W. Moriarty, B. Eiteneer, M. Goldenberg, C. T. Bowman, R. K. Hanson, S. Song, W. C. Gardiner, Jr., V. V. Lissianski, Z. Qin, *GRI-Mech* 3.0, 2018.
- [48] D. G. Goodwin, H. K. Moffat, R. L. Speth, *Cantera: An Object-Oriented Software Toolkit For Chemical Kinetics, Thermodynamics, And Transport Processes*. Version 2.3.0, 2017.

- [49] M. D. Smooke, *Journal of Computational Physics* 48 (1982) 72–105.
- [50] B. Tian, Y. Gao, C. Zhang, S. Hochgreb, *Combustion and Flame* 192 (2018) 224–237.
- [51] B. Tian, C. Zhang, Y. Gao, S. Hochgreb, *Aerosol Science and Technology* (DOI: 10.1080/02786826.2017.1366644, 2017).
- [52] J. H. Kent, D. R. Honnery, *Combustion and Flame* 79 (1990) 287–298.
- [53] D. R. Honnery, J. H. Kent, *Combustion and Flame* 82 (1990) 426–434.
- [54] F. G. Roper, *Combustion and Flame* 29 (1977) 219–226.
- [55] R. M. Williams, A. A. Westenberg, *Flame Structure*, McGraw-Hill, New York and London, 1965.
- [56] R. T. Jacobsen, E. W. Lemmon, *International Journal of Thermophysics* 25 (2004) 21–69.
- [57] W. Sutherland, *Philosophical Magazine S. 5.* (1893) 507–531.
- [58] D. of Engineering of Crane Co., *Flow of Fluids Through Valves, Fittings, and Pipe*, Crane Co., Connecticut USA, 2009.
- [59] C. Guéret, M. Daroux, F. Billaud, *Chemical Engineering Science* 52 (1997) 815–827.
- [60] a. Burcat, R. Branko, *Technical Report ANL-05/20* (2005) ANL-05/20 TAE 960.

- [61] O. Kubaschewski, A. L. Evans, C. B. Alcock, Metallurgical thermochemistry, Oxford, 4 edition, 1967.
- [62] J. Chipman, Metallurgical and Materials Transactions B 3 (1972) 55–64.
- [63] M. Fulem, K. Ružicka, C. Cervinka, M. Alves da Rocha, L. Santos, R. Berg, The Journal of Chemical Thermodynamics 57 (2013) 530–540.
- [64] N. R. Pradhan, H. Duan, J. Liang, G. S. Iannacchione, Nanotechnology 20 (2009) 245705.
- [65] G. J. Kabo, E. Paulechka, A. V. Blokhin, O. V. Voitkevich, T. Liavitskaya, A. G. Kabo, Journal of Chemical Engineering Data 61 (2016) 3849–3857.
- [66] K. Sasaki, Y. Teraoka, Journal of The Electrochemical Society 150 (2003) A878–A884.
- [67] D. L. A. de Faria, S. Venâncio Silva, M. T. de Oliveira, Journal of Raman Spectroscopy 28 (1997) 873–878.
- [68] L. Slavov, M. V. Abrashev, T. Merodiiska, C. Gelev, R. E. Vandenberghe, I. Markova-Deneva, I. Nedkov, Journal of Magnetism and Magnetic Materials 322 (2010) 1904–1911.
- [69] M. S. Dresselhaus, G. Dresselhaus, R. Saito, A. Jorio, Physics Reports 409 (2005) 47–99.
- [70] A. Sadezky, H. Muckenhuber, H. Grothe, R. Niessner, U. Pöschl, Carbon 43 (2005) 1731–1742.

- [71] S. D. M. Brown, A. Jorio, P. Corio, M. S. Dresselhaus, G. Dresselhaus, R. Saito, K. Kneipp, *Phys. Rev. B* 63 (2001) 155414.
- [72] A. Jorio, M. A. Pimenta, A. G. S. Filho, R. Saito, G. Dresselhaus, M. S. Dresselhaus, *New Journal of Physics* 5 (2003) 139–139.
- [73] C. Hoecker, F. Smail, M. Bajada, M. Pick, A. Boies, *Carbon* 96 (2016) 116–124.
- [74] J. Oudar, *Catalysis Reviews* 22 (1980) 171–195.